Radio continuum properties of young planetary nebulae

L. Cerrigone,[1]⋆ G. Umana,[2] C. Trigilio,[2] P. Leto,[3] C. S. Buemi[2] and J. L. Hora[1]

[1]*Harvard-Smithsonian Center for Astrophysics, 60 Garden St, MS-65, Cambridge, MA 02138, USA*
[2]*INAF-Osservatorio Astrofisico di Catania, via S. Sofia 78, 95123 Catania, Italy*
[3]*INAF-Istituto di Radioastronomia, C.P. 161, Noto, Italy*

ABSTRACT

We have selected a small sample of post-AGB (Asymptotic Giant Branch) stars in transition towards the planetary nebula and present new Very Large Array multi-frequency high-angular resolution radio observations of them. The multi-frequency data are used to create and model the targets' radio continuum spectra, proving that these stars started their evolution as very young planetary nebulae. In the optically thin range, the slopes are compatible with the expected spectral index (-0.1). Two targets (IRAS 18062+2410 and 17423−1755) seem to be optically thick even at high frequency, as observed in a handful of other post-AGB stars in the literature, while a third one (IRAS 20462+3416) shows a possible contribution from cold dust. In IRAS 18062+2410, where we have three observations spanning a period of four years, we detect an increase in its flux density, similar to that observed in CRL 618.

High-angular resolution imaging shows bipolar structures that may be due to circumstellar tori, although a different hypothesis (i.e. jets) could also explain the observations. Further observations and monitoring of these sources will enable us to test the current evolutionary models of planetary nebulae.

Key words: stars: AGB and post-AGB – planetary nebulae: general – radio continuum: stars.

1 INTRODUCTION

The evolution of planetary nebulae (PN) remains a challenging topic in astrophysics. Several studies have focused on the link between the post-Asymptotic Giant Branch (AGB) and PN phases to investigate the changes that occur in the evolutionary stage between these object classes. PN have been observed over a wide wavelength range, from X-ray to radio frequencies. Their complex morphologies and the shaping mechanisms that produced them are still a matter of debate. Companion stars, jets from central stars, magnetic fields, dust tori and interacting winds are some of the possible shaping agents suggested as being responsible for various PN morphologies, and an overlap of their actions cannot be ruled out.

Hubble Space Telescope (*HST*) imaging has demonstrated that pre-PN show non-spherical symmetry even at late spectral types, which implies that the shaping process in these sources starts very early after the AGB (Balick & Frank 2002). Non-spherically symmetric structures have also been observed in AGB stars that are part of a binary system (Karovska et al. 2007), which could indicate that some shaping agents are already active in this evolutionary phase. In general, the current theory of PN evolution is based on the Interacting Stellar Wind (ISW) model (Kwok, Purton & Fitzgerald 1978) and its generalized version (Kahn & West 1985). However, this model does not account for shaping because it assumes that an asymmetric distribution of matter is already present when the wind

interaction occurs. Other models take into account the possible role of jets, and have been successfully applied to some nebulae (Sahai & Trauger 1998). It has been suggested that the interaction with a companion object, even a massive planet, may provide the necessary asymmetry (Soker 2006). Also, large-scale magnetic fields, influencing or determining the shapes, might be sustained by a dynamo process (Blackman et al. 2001).

The birth of a PN is defined by the observation of an ionization front, which is itself a shaping agent and could heavily influence the morphology established in earlier evolutionary phases, disrupting the molecular and dust circumstellar shells. Near- and mid-infrared images of PN, which trace the molecular and warm dust emission, have been compared to optical line images, which trace the ionized elements, and have shown the presence of similar structures (Latter et al. 1995). Therefore, it seems that molecular and ionized gas and dust grains can spatially co-exist in these sources. This makes the investigation of the spatial distribution and physical properties of the ionized component in these envelopes even more compelling.

In this context, important information can be provided by observations of very young PN or pre-PN, where the physical processes associated with PN formation are still occurring. To investigate the properties of these rare objects in transition from the post-AGB to PN, we have selected a sample of pre-PN and searched for radio emission from ionized shells. The targets were selected from stars classified in the literature as hot post-AGB candidates, showing strong far-infrared excess and B spectral-type features. We detected radio emission in 10 sources in the selected sample (Umana et al.

⋆E-mail: lcerrigone@cfa.harvard.edu

Table 1. Summary of all the performed observation runs.

Date	VLA conf.	Freq. (GHz)	Flux calibr.	Targets
Low angular resolution				
2003				
February 15	D	1.4, 4.8, 8.4, 14.9, 22.4	3C286	18062+2410
				17423−1755
				17460−3114
				20462+3416
February 16	D	1.4, 4.8, 8.4, 14.9, 22.4	3C286	20462+3416
				19336−0400
				18442−1144
				19590−1249
March 8	D	1.4, 4.8, 8.4, 14.9, 22.4	3C286	17381−1616
				17460−3114
				18062+2410
March 21	D	1.4, 4.8, 8.4, 14.9, 22.4	3C48	06556−1623
2004				
April 18	C	8.4	3C48	22023+5249
2005				
July 25	C	1.4	3C48	18062+2410
				19336−0400
				19590−1249
July 26	C	1.4, 8.4	3C48	18062+2410
				19336−0400
				19590−1249
				20462+3416
High-angular resolution				
2003				
July 10	A	8.4	3C48	18062+2410
				18442−1144
				19590−1249
				19336−0400
August 15	A	8.4	3C48	17381−1616
2004				
October 29	A	8.4	3C286	22023+5249

2004). The detection of radio continuum emission is proof of the presence of free electrons and therefore of an ionized shell.

For a better understanding of these sources, we have performed a multi-frequency follow-up to build up radio continuum spectra and collect information about the physical conditions in the nebulae. Several nebular parameters can be determined by radio flux density measurements (for example, electron density and ionized mass) but most calculations rely on the assumption of an optically thin emission. Although this is presumably the case for observations at frequencies higher than 5 GHz, only the construction of the whole centimetre continuum spectrum can enable us to distinguish between optically thick and thin regimes. Very Large Array (VLA) observations have also given us insight in the morphologies of the envelopes.

2 OBSERVATIONS AND RESULTS

2.1 Low-angular resolution observations

Multi-frequency observations were carried out at the VLA, managed by National Radio Astronomy Observatory (NRAO), in several

runs, at 1.4, 4.8, 8.4, 14.9 and 22.4 GHz (respectively 20, 6, 3.6, 2 and 1.3 cm), in D and C arrays, to inspect the spectral energy distribution in the radio range. Table 1 lists the observation details. The 8.4-GHz observations were performed in 2001 (Umana et al. 2004). During the 2003 runs, strong interference led to the failure of almost all of the 1.4-GHz observations and part of the 14.9-GHz ones. To acquire information about the lower frequency range of the spectrum of four sources (namely IRAS 18062+2410, 19336−0400, 19590−1249, 20462+3114), observations were performed in 2005 at both 1.4 and 8.4 GHz; the latter ones enabled us to check for any intrinsic variation in the emitted flux. Although these latter runs were carried out in a different array configuration (with a smaller synthesized beam), this cannot cause missing flux, since all of our sources are point-like in both D and C arrays at any frequency. The Largest Angular Scale (LAS)[1] is much larger than the typical sizes of these objects ($\leq$2 arcsec) even at the shortest wavelength, being 60 arcsec at 22.4 GHz (D and C arrays have the same LAS). The nominal beam sizes in D array are 44, 14, 8.4,

---

[1] The LAS is the size of the largest structure that an interferometer can map.

Table 2. Flux densities and their errors (including a 5 per cent absolute flux-density calibration error) from our D and C array observation runs are shown for each source and frequency. The asterisks indicate the sources chosen for high-angular resolution imaging. The spectral indexes in the optically thin range and the rms in the high-angular resolution maps are also shown.

| IRAS ID | Flux density (mJy) | | | | | Spectral index | A array rms (mJy) | A array beam size (arcsec) |
	1.4 GHz	4.8 GHz	8.4 GHz	14.9 GHz	22.4 GHz		8.4 GHz	8.4 GHz
06556−1623	2.0 ± 0.1^a	0.60 ± 0.04	0.55 ± 0.03	0.43 ± 0.09	0.36 ± 0.06	-0.29 ± 0.20	–	–
17381−1616*	1.1 ± 0.1	1.61 ± 0.09	1.42 ± 0.09	1.3 ± 0.1	1.19 ± 0.08	-0.20 ± 0.11	0.038	0.26
17423−1755	$-^b$	1.74 ± 0.06^a	0.26 ± 0.03	$-^b$	0.75 ± 0.08	$+1.08^e$	–	–
17460−3114*	$-^b$	1.6 ± 0.1	1.29 ± 0.08	1.7 ± 0.1	1.24 ± 0.08	-0.10 ± 0.12	–	–
18062+2410*	0.26 ± 0.04^c	1.27 ± 0.07	1.46 ± 0.09^d	$-^b$	1.8 ± 0.1	$+0.22 \pm 0.10$	0.045	0.22
18442−1144*	$-^b$	17.8 ± 0.9	19.2 ± 0.9	14.2 ± 0.7	13.5 ± 0.7	-0.22 ± 0.09	0.038	0.28
19336−0400*	8.0 ± 0.4^c	10.4 ± 0.5	9.7 ± 0.5	8.0 ± 0.4	7.0 ± 0.3	-0.26 ± 0.09	0.034	0.27
19590−1249*	3.2 ± 0.2^c	3.1 ± 0.2	2.8 ± 0.1	2.3 ± 0.1	2.1 ± 0.1	-0.26 ± 0.10	0.028	0.32
20462+3416	0.48 ± 0.06^c	0.60 ± 0.05	0.42 ± 0.05	0.50 ± 0.09	0.83 ± 0.07	-0.02 ± 0.17^f	–	–
22023+5249	–	–	2.0 ± 0.1	–	–	–	0.027	0.29

^{a}More than one source in the beam: the flux density must be regarded as an upper limit.
^{b}The data were not recovered.
^{c}The measurement was performed in 2005.
^{d}In 2005, the flux density was 2.1 ± 0.1 mJy.
^{e}This value is calculated with two data points only.
^{f}The 22.4-GHz point was not included in the fitting procedure.

3.9 and 2.8 arcsec, while in C array they are 12.5, 3.9, 2.3, 1.2 and 0.9 arcsec, respectively at 1.4, 4.8, 8.4, 14.9 and 22.4 GHz. One of the nebulae detected in 2001 (18371−3159) could not be observed because of limited observation time.

A typical observing scan consisted of two 15-min pointings on target, preceded and followed by 1-min scans on the phase calibrator. For a better phase calibration, 22.4-GHz observations were carried out pointing at the target for four 7-min scans alternating with 1-min scans on the phase calibrator.

The data were reduced with the Astronomical Image Processing System (AIPS), according to the recommended reduction process: the data set was FILMMED into AIPS with average opacity correction and nominal sensitivities (*doweight* = 1), edited to flag interference or any other bad points and calibrated along with point weights (*docalib* = 2). Maps were obtained using the task IMAGR with natural weights and cleaned down to the theoretical rms noise whenever possible, performing some hundreds of iterations of the CLEAN algorithm. The flux density for each source in every map was estimated by fitting a Gaussian to the unresolved source (task JMFIT), and the rms noise was calculated in an area much larger than the synthesized beam (>100 beam), without evident sources in it (task IMEAN).

For IRAS 17423−1755 and 06556+1623, a second nearby (within 40 arcsec) source was detected and large-wavelength data cannot be considered indicative of their flux densities because of confusion problems. Tables 1 and 2 summarize the observation runs and the flux density measurements obtained. The reported error has been calculated as $\sigma = \sqrt{\mathrm{rms}^2 + (\sigma_{\mathrm{cal}} S_\nu)^2}$, where σ_{cal} is a 5 per cent absolute calibration error.

2.2 High-angular resolution observations

To inspect the morphology of our targets, we carried out observations at 8.4 GHz in A array at the VLA for those sources that were brighter than 1 mJy at this frequency in our detection experiment reported in Umana et al. (2004): IRAS 17381−1616, 18062+2410, 18442−1144, 19336−0400 and 19590−1249. The 1 mJy limit was set to select nebulae with surface brightnesses high enough to be imaged with the A array. The angular resolution of these observa-

tions was ∼0.2 arcsec. Two runs were performed in 2003: the first on July 10 (UT 07:04:50; 10:29:30) and the second one on August 15 (UT 05:12:30; 06:37:50). The integration time per object was about 1.5 h. The reduction process followed the standard format, as reported in the previous section. In the task IMAGR, the pixel size was set to 0.05 arcsec, so that the convolution beam is at least three pixels wide; Brigg's weighting of the data was used to find a good compromise between sensitivity and resolution (*robust* = 0) for all the resolved sources except 19590−1249, as natural weights were necessary in order not to miss its faint emission. For 17381−1616 and 18062+2410, we set, respectively, *robust* = −2 and −4 (nearly pure uniform weighting) to increase the resolution. The number of clean iterations was set to 1000, *minpatch* 127 and *gain* 0.1. The absolute calibrator was 3C48, its flux density set to 3.15 Jy. On 2004 October 29, we also managed to perform a snapshot (15 min on source) in A array of IRAS 22023+5249, which we had detected as a radio source in a previous observation run in C array and had measured as 2.0 ± 0.1 mJy (including absolute flux density calibration error).

All the selected targets showed clear bipolar structures except IRAS 17381−1616 and 18062+2410, which were barely (IRAS 17381−1616) or not (IRAS 18062+2410) resolved. Fig. 1 shows the structures found in all the radio envelopes as observed with the A array.

3 RADIO PROPERTIES

3.1 Modelling

We have modelled the radio continuum spectra assuming that the central star is surrounded by a shell of ionized gas with density radially decreasing as r^{-2}. We have calculated a 3D distribution of mass in a spherical shell with outer radius R_{out}, inner radius $R_{\mathrm{in}} = \eta R_{\mathrm{out}}$ (with $0 < \eta < 1$) and density at the inner radius ρ_{in}. The calculation of the average density in the shell links this parameter to the density at the inner radius: $\langle \rho \rangle \approx \eta^2 (1 - \eta) \rho_{\mathrm{in}}$. The electron temperature was set to 10^4 K for all nebulae. Details of the radio model can be found in Umana et al. (2008).

(a) 17381-1616

(b) 18062+2410

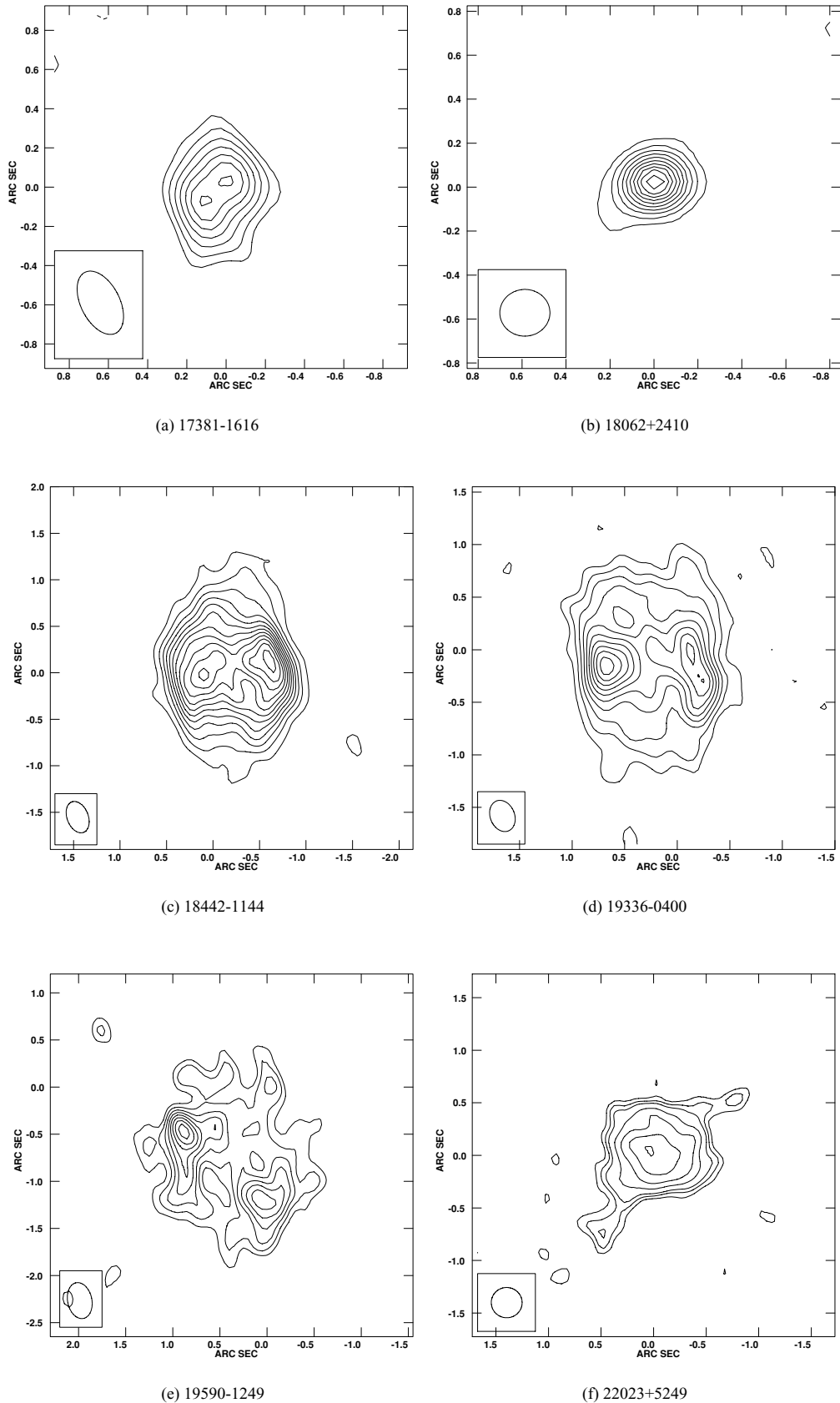(c) 18442-1144

(d) 19336-0400

(e) 19590-1249

(f) 22023+5249

Figure 1. Radio maps at 8.4 GHz of the targets observed in high angular resolution. The flux density levels, in units of μJy beam^{-1}, are: in 17381 $(-3, 3, 4, 5, 6, 7, 8, 9)\sigma$; in 18062 $(-3, 3, 6, 9, 12, 15, 18, 21, 24, 27, 30)\sigma$; in 18442 $(-3, 3, 6, 9, 12, 15, 18, 21, 24, 27, 30, 33, 36)\sigma$; in 19336 $(-3, 3, 5, 7, 9, 11, 13, 15, 17, 19, 21)\sigma$; in 19590 $(-3, 3, 4, 5, 6, 7, 8, 9, 10)\sigma$ and in 22023 $(-3, 3, 4, 5, 7, 9, 11, 13)\sigma$; where σ indicates the rms calculated in each map and listed in Table 2. The maps do not show any negative level, because no such levels are present in the mapped areas.

Table 3. Model parameters for the radio shells. IRAS 18062+2410 was modelled as an emitting sphere, not a shell.

Target	Distance kpc	R_{out} arcsec	R_{in}/R_{out}	ρ_{in} 10^4 cm^{-3}	$\langle\rho\rangle$ 10^3 cm^{-3}	M_{ion} 10^{-4} M$_\odot$
06556−1623	1	0.5	0.15	15	3	0.1
17381−1616	1	0.35	0.195	30	9	0.14
17460−3114	1	1.1	0.049	40	0.9	0.4
18062+2410	6.4[a]	0.061	–	25	8	1.7
18442−1144	4	1	0.225	8.8	3.5	77
19336−0400	4	1	0.2	8	2.6	57
19590−1249	4[b]	1.2	0.28	2	1.1	40
20462+3416	3[c]	1.1	0.11	4	0.04	5

[a]Bogdanov (2000).
[b]Conlon et al. (1993).
[c]Arkhipova et al. (2001).

Only a few estimates of the distances to the stars in our sample are available. Where available in the literature, we have used the most common estimates of this parameter. For IRAS 18442−1244 and 19336−0400, since their sizes and flux densities are comparable to what detected in IRAS 19590−1249, we assume the same distance as for this source. For the remaining targets, we have adopted a standard value of 1 kpc as an estimate of the order of magnitude of their distances. Our radio model code requires as an input the distance to the star as well as the density at the inner radius of the shell, outer radius of the ionized shell, inner to outer radius ratio, and electron temperature. For the outer radii, we have assumed as upper limits the sizes estimated in Umana et al. (2004), which were calculated from the VLA theoretical angular resolution. For those objects that were observed with the VLA in A array (IRAS 17381−1616, 18062+2410, 18442−1144, 19336−0400, and 19590−1249),[2] we used our estimate of their radii, based on their 3σ size. For IRAS 18062+2410, it was necessary to use a different geometry, since with a shell structure we could not model a steep enough increase of flux density in the optically thick range. Therefore, we used a sphere instead of a spherical shell.

The results of our radio models are reported in Table 3. The density and ionized mass values are in agreement with those expected for young PN. For example, in NGC 7027, a high excitation young PN, values of 10^4 cm^{-3} and 0.005 M$_\odot$ have been measured (Bains et al. 2003), although even in this very well-studied PN, these results suffer from the distance uncertainty. Such distance independent parameters as emission measure and brightness temperature have been previously calculated for our targets (Umana et al. 2004) and found to match the expected values for young PN.

We notice that in some cases the data points, especially at higher frequency, seem to show a steeper than expected slope in the optically thin range ($S_\nu \sim \nu^{-0.1}$). Besides our modelling, we estimated the empirical spectral indexes by a linear fitting (in the log–log plane) of the data points that correspond to the optically thin regime (typically 4.8–22.4 GHz data). The results of the fitting are summarized in Table 2.

Because at high frequency (14.9 and 22.4 GHz) a lack of short baselines may cause a lower sensitivity to flux from extended structures (therefore a lower total flux density), we checked whether tapering our data (i.e. assigning larger weights to short baselines)

could lead to larger flux densities, thus making the slopes in the spectra less steep. We did not find any significant difference in the results from tapered and non-tapered data. The empirical spectral indexes of three of the targets (IRAS 06556−1623, 17381−1616, and 17460−3114) are close to the expected value of −0.1, and out of the expected range for three others (IRAS 18442−1144, 19336−0400 and 19590−1249). Although we cannot rule out that the observed steeper slopes might be real and further observations should be carried out, if we consider that the reported errors are based on a statistics on four points only, the deviation from −0.1 is not statistically significant. Therefore, we conclude that, within the errors, the spectral indexes are compatible with their expected value.

Fig. 2 shows the data points obtained in our VLA runs, the model spectra and the linear fitting. We have not included IRAS 17423−1755 in our modelling because only two data points are available. The flux density values obtained for this target would indicate an optically thick spectrum up to 22 GHz.

Another particular result is the spectrum of IRAS 20462+3416, which is well matched by the model in the 1–15 GHz range, while the 22.4-GHz point is higher than the others. Since the measured radio flux densities are all below 1 mJy, even a small contribution from cold dust may be non-negligible and so explain the 22.4-GHz result. Observations in the mm and sub-mm ranges would assess whether such a cold dust component is present or not.

3.2 IRAS 18062+2410

In our modelling, we have used data from 2001, 2003, and 2005, since the sources that were re-observed in 2005 (see above) did not show any flux-density variation with respect to the 2001 8.4-GHz results, within observational errors. The only exception is IRAS 18062+2410, whose flux density varied by about +44 per cent, increasing from 1.46 ± 0.09 in 2001 to 2.1 ± 0.1 mJy in 2005, while its secondary calibrator, 1753+288, varied from 0.82 ± 0.03 Jy in 2001 to 1.41 ± 0.04 Jy in 2005 (+75 per cent). Unfortunately, it was not possible to use the same primary calibrator in the two runs (see Table 1), which introduces a different density scale for the two measurements, although the error should be within a few percent (3–5 per cent). The flux-density variation in the secondary calibrator might indicate issues with the flux density calibration. Since other targets were also observed in the same run and no change was measured in their flux densities within the observational uncertainties, we conclude that the variation observed in 1753+288

---

[2] We do not have multi-frequency observations of IRAS 22023+5249, since we had not radio detected this target at the time of our multi-frequency run.
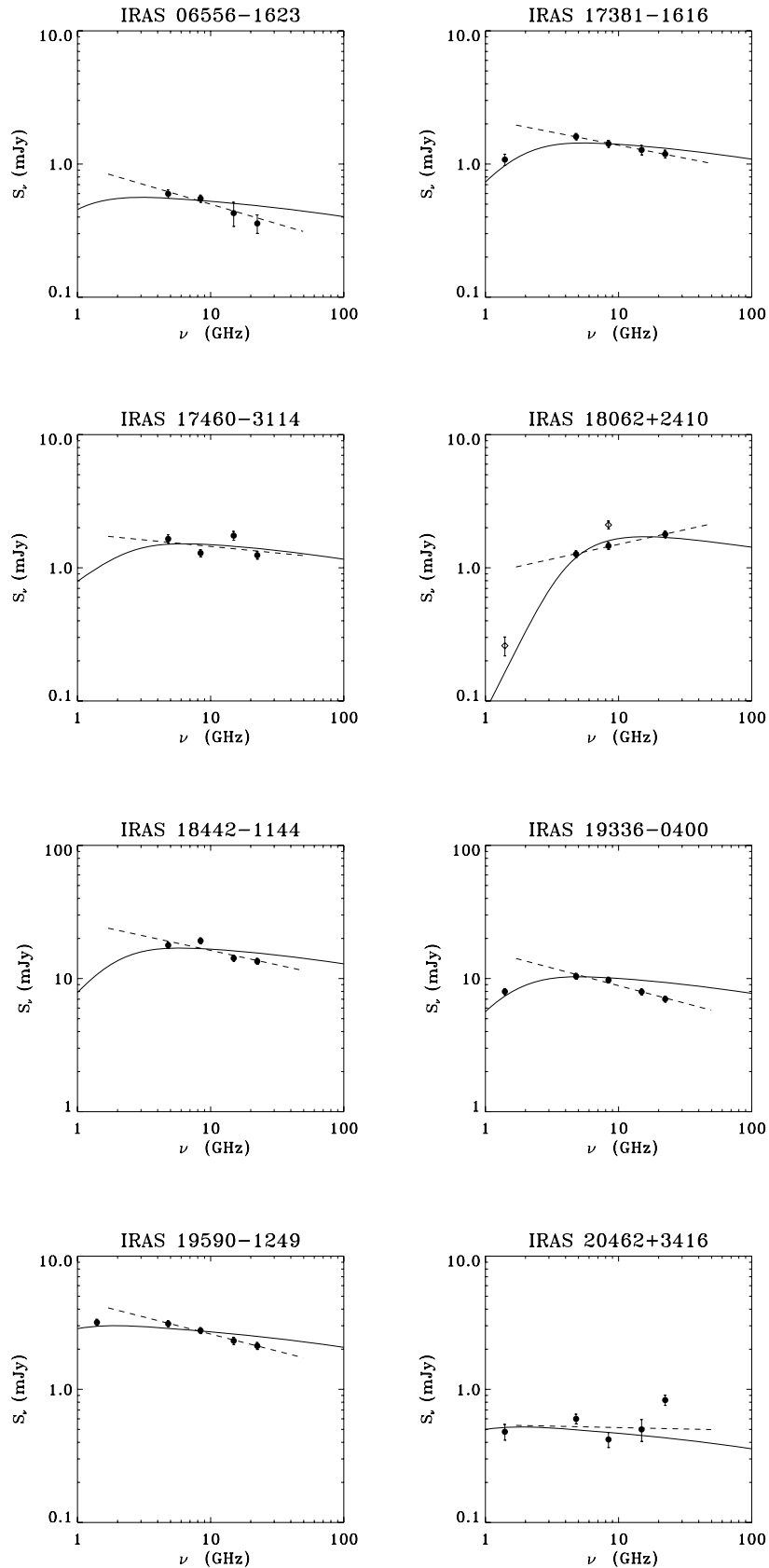
Figure 2. Plots of the multi-frequency data obtained at the VLA. For 18062+2410, 19336−0400, 19590−1249, and 20462+3416, 2005 1.4-GHz data points have also been used. In 18062, they have been overplotted as diamonds. The dashed lines are the result of the linear (in the log–log plane) fitting of the optically thin range points. The plots therefore show the difference between the modelled (solid line) and empirical (dashed line) dependence on frequency. The error bars are in some cases within the size of the data points.
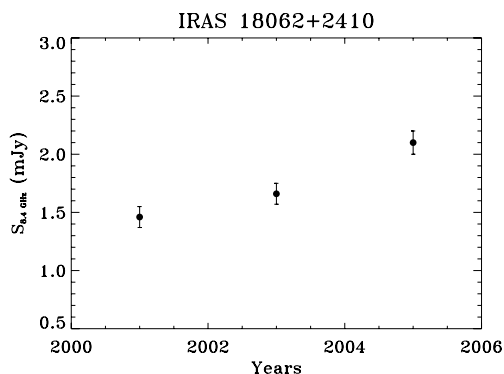
Figure 3. Increase of the 8.4-GHz flux density in IRAS 18062+2410 during years 2001–2005.

is real, as possible for a secondary calibrator, but it does not account for the variation observed in the target object. When we combine all of our observations of this target, including our 2003 measurement (A array data set) of 1.66 ± 0.09 mJy, we can conclude that the radio flux density of IRAS 18062+2410 has increased during the period we have monitored it (see Fig. 3).

A similar uncommon increase of the radio flux density was detected in CRL 618 from 1975 to 1991 (Knapp et al. 1995). If, as observed in CRL 618, we assume a linear increase, we can fit the three points in Fig. 3 and extrapolate that the ionization in IRAS 18062+2410 started around 1991, confirming the rapid evolution previously observed in this object (Parthasarathy et al. 2000; Arkhipova et al. 2001).

The spherical model used in modelling this object allowed us to match the 2003 data, using the 2005 1.4-GHz value as an upper limit. We determine that the shell in this target is optically thick beyond 5 GHz. Similar behaviour has been observed in CRL 618 also (Knapp et al. 1995). Further observations, in both the radio and at other wavelengths, will help us to determine whether these objects share other common features.

3.3 Radio morphology

Fig. 1 shows the structures observed in the resolved targets. All except IRAS 18062+2410 show bipolar radio morphology, with clearly resolved peaks. IRAS 17381−1616 shows a hint of bipolarity, although the angular resolution is not adequate to show its morphology. Aaquist & Kwok (1991) also observed a sample of young PN with high resolution in the radio and found that most of their targets had a bipolar structure. Such radio morphologies, to be set in the standard ISW scenario, require a strong density gradient in the nebula, with higher density regions perpendicular to the main axis of the nebula (Aaquist & Kwok 1996). Following this interpretation, the two bright peaks of emission are due to an opacity effect, with the optically thin radio flux tracing higher density regions. The other possibility is that we are actually observing the very early onset of outflows/jets piercing the circumstellar envelope, as evident in many *HST* images of pre-PN (Sahai & Trauger 1998) and also pointed out by high-resolution CO observations of the molecular component of the envelope (Huggins et al. 2000). However, it is difficult to interpret the morphology observed in IRAS 22023+5349 in the framework of the standard ISW model, even invoking a strong density gradient in the nebula. For this object, a jet would be a more likely source of the observed morphology.

4 SUMMARY

We have presented radio continuum observations of a small sample of pre-PN. The observations were carried out to inspect both the morphology and the physical conditions of the ionized component in these nebulae. Compact PN are, in principle, only one possible explanation for radio-frequency continuum emission from evolved stars, the others being stellar photosphere, chromosphere and circumstellar dust (Knapp et al. 1995). Our observations rule out the possibility of a stellar wind or dust origin for the emission, since the obtained spectra are not compatible with such hypotheses. The dust would exhibit an approximate blackbody spectrum ($S_\nu \propto \nu^2$ in the radio range), and a stellar wind would have a 0.6 spectral index over a wide range of frequencies (Panagia & Felli 1975). We have modelled the observed spectra assuming that the emission arises in spherical shells around the central stars, with the density decreasing as r^{-2}. The values of electron densities and ionized masses found for our targets confirm their nature as young PN, since they fall within the ranges expected for such objects. The data seem to point to a somewhat steeper than expected slope beyond 5 GHz but, by spectral fitting, we calculated spectral indexes that match, to within errors, the theoretical value of -0.1.

IRAS 18062+2410 appears to be optically thick up to 8.4 GHz and also shows flux-density variations on a time-scale of a few years. Such variations are rarely observed in the post-AGB/young-PN transition phase and indicate that this star belongs to a group of objects having such properties as those observed in CRL 618. IRAS 17423−1755 also seems to be optically thick at high frequency, but the complete spectrum is needed to confirm this result. Quite interestingly, IRAS 20462+3416, whose overall centimetre spectrum is very flat, has a larger flux density at 22.4 GHz than at lower frequencies. We speculate that this may be due to a contribution from cold dust.

The high-angular resolution observations that we have presented show that the ionization in these targets has already involved the walls of the cavity around the central star and is not limited to the tenuous gas within the cavity. All of the targets have been at least partly resolved, except IRAS 18062+2410. Almost all of the envelopes show two peaks of emission in a somewhat extended nebulosity that can be explained as an opacity effect, possibly due to a circumstellar torus, or the onset of jets. Unlike the other targets, the envelope in IRAS 22023+5249 shows more of an elongation along an axis than two bright peaks. Such a morphology would be better explained by the action of jets rather than the presence of a torus.

REFERENCES

Aaquist O. B., Kwok S., 1991, ApJ, 378, 599
Aaquist O. B., Kwok S., 1996, ApJ, 462, 813
Arkhipova V. P., Ikonnikova N. P., Noskova R. I., Kommisarova G. V., Klochkova V. G., Esipov V. F., 2001, Astron. Letters, 27, 719
Bains I., Bryce M., Mellema G., Redman M. P., Thomasson P., 2003, MNRAS, 340, 381

Balick B., Frank A., 2002, ARA&A, 40, 439

Blackman E. G., Frank A., Markiel J. A., Thomas J. H., Van Horn H. M., 2001, Nat, 409, 485

Bogdanov M. B., 2000, Astron. Rep., 44, 685

Conlon E. S., Dufton P. L., McCausland R. J. H., Keenan F. P., 1993, ApJ, 408, 593

Huggins P. J., Forveille T., Bachiller R., Cox P., 2000, ApJ, 544, 889

Kahn F. D., West K. A., 1985, MNRAS, 212, 837

Karovska M., Carilli C. L., Raymond J. C., Mattei J. A., 2007, ApJ, 661, 1048

Kwok S., Purton C. R., Fitzgerald P. M., 1978, ApJ, 219, L125

Knapp G. R., Bowers P. F., Young K., Phillips T. G., 1995, ApJ, 455, 293

Latter W. B., Kelly D. M., Hora J. L., Deutsch L. K., 1995, ApJ, 100, 159

Panagia A., Felli M., 1975, A&A, 39, 1

Parthasarathy M., García-Lario P., Sivarani T., Manchado A., Sanz Fernández de Córdoba L., 2000, A&A, 357, 241

Sahai R., Trauger J. T., 1998, AJ, 116, 1357

Soker N., 2006, ApJ, 645, L57

Umana G., Cerrigone L., Trigilio C., Zappalà R. A., 2004, A&A, 428, 121

Umana G., Trigilio C., Cerrigone L., Leto P., Buemi C. S., 2008, MNRAS, 386, 1404

This paper has been typeset from a TEX/LATEX file prepared by the author.